International Journal of Microwave and Wireless Technologies

cambridge.org/mrf

Low-profile dual-CP antenna array using spiral sequential rotation technique for satellite communication

Zhan Yu Kang[1,2], Lianxing He[3], Shaokang Pan[4], Dongliang Fei[3] and Guang Liang[3]

[1]Innovation Academy for Microsatellites, Chinese Academy of Sciences (IAMCAS), Shanghai, China; [2]University of Chinese Academy of Sciences (UCAS), Beijing, China; [3]Shanghai Engineering Center for Microsatellites, Shanghai, China and [4]School of Information Science and Technology, ShanghaiTech University, Shanghai, China

Research Paper

Cite this article: Kang ZY, He L, Pan S, Fei D, Liang G (2025) Low-profile dual-CP antenna array using spiral sequential rotation technique for satellite communication. *International Journal of Microwave and Wireless Technologies* **17**(10), 1865–1874. https://doi.org/10.1017/S175907872510281X

Received: 21 July 2025
Revised: 15 December 2025
Accepted: 17 December 2025

Keywords:
cross-polarization level (XPL); dual-circular polarization (CP); low-profile; satellite application; spiral sequential rotation (SSR)

Corresponding author: Lianxing He;
Email: 13816474811@139.com

Abstract

A low-profile dual-circularly polarized (CP) antenna array using spiral sequential rotation (SSR) technique is proposed. The array element consists of two stacked CP patches and a double-layer ceramic substrate with high dielectric constant. Dual CP radiations are accomplished by the slender rectangular structures on the radiators, which can excite two orthogonal characteristic modes. An extremely small size of $0.005\lambda^3$ (λ is the wavelength in free space for the low bands) and a wide 3-dB axial ratio beamwidth (ARBW) of 206° are achieved. Furthermore, the SSR technique is employed to achieve low cross-polarization level (XPL) within a large scanning angle. Prototype of a 6 × 6 array was fabricated and measured. Experimental results demonstrate that a wide 3-dB AR scanning angle of ± 55° is realized for LHCP as well as RHCP radiation. Additionally, low XPL less than −18.1 dB with gain fluctuation less than 4 dB are achieved over −55° ∼ + 55°. Meanwhile, the array has successfully passed the mechanical test and the thermal vacuum test (−90° ∼ + 90°). All the merits of dual-CP radiation, extremely low profile of 0.06λ, wide 3-dB AR scanning capability, and low XPL make our proposed dual-CP SSR antenna array be attractive candidate for satellite applications.

Introduction

In satellite communications, circularly polarized (CP) antennas are highly demanded due to their several unique advantages, such as ability to overcome the Faraday effect in ionosphere [1] and polarization distortion elimination [2]. In particular, dual-CP shared-aperture antenna arrays have received extensive attention because of their compact aperture area and low system costs, which can save valuable space resources of satellite system [3–6]. Microstrip antenna arrays can be competitive candidate due to their low profile [7–11]. However, the axial ratio beamwidth (ARBW) of elements is usually limited, which may restrict the scanning coverage. Cavity-backed antennas with wide ARBW were proposed [12, 13], while they typically need relatively large horizontal dimensions, making it difficult to meet the element spacing requirement for wide-scanning array. Shorting PINs loaded on the radiating patch can control the beamwidth [14, 15]. Nevertheless, electronic components are normally not recommended for being exposed in the harsh space environment. In addition, poor cross-polarization level (XPL) can be a problem due to the regular arrangement of antenna elements. Rotated technique such as sequentially rotated technique (SRT) [16–18] is normally adopted to achieve a better scanning performance.

In this paper, a low-profile L-band dual-CP antenna array using spiral sequential rotation (SSR) technique is proposed. Stacked antenna element with wide 3-dB ARBW of 206° is presented to realize right-hand CP (RHCP) for downlink frequency band (1710–1730 MHz) and left-hand CP (LHCP) for uplink frequency band (1800–1820 MHz). Extremely small size of $0.005\lambda^3$ is achieved by using the ceramic substrate with high dielectric constant. Furthermore, the SSR technique is applied to achieve low XPL across a large scanning angle. A 6 × 6 array prototype was fabricated and measured for validation. Measured results show that a wide 3-dB AR scanning angle of ± 55° is realized for LHCP as well as RHCP radiation. Additionally, low XPL with gain fluctuation less than 4 dB is achieved over wide-scanning angle of −55° ∼ + 55°. Moreover, the array has successfully passed the mechanical test and the thermal vacuum test (−90° ∼ + 90°). With the dual-CP radiation capability, ultra-low profile of 0.06λ, wide 3-dB AR scanning angle, and low XPL, the proposed dual-CP SSR array is a highly attractive candidate for satellite communication applications.

© The Author(s), 2026. Published by Cambridge University Press in association with The European Microwave Association.

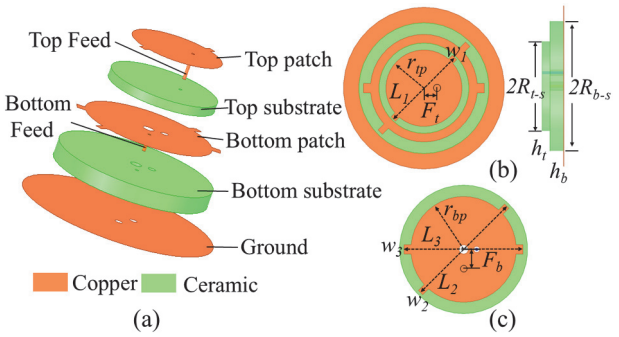


Figure 1. (a) Exploded view, and (b) top and side views of the proposed dual-CP element, and (c) top view of bottom patch (rtp = 12.2 mm, rbp = 17.1 mm, Rt-s = 14.6 mm, Rb-s = 21.1 mm, L1 = 28 mm, L2 = 40.8 mm, L3 = 39 mm, w1 = w2 = 2 mm, w3 = 3 mm, Ft = 4.3 mm, Fb = 5.5 mm, ht = 2.5 mm, hb = 4.5 mm).

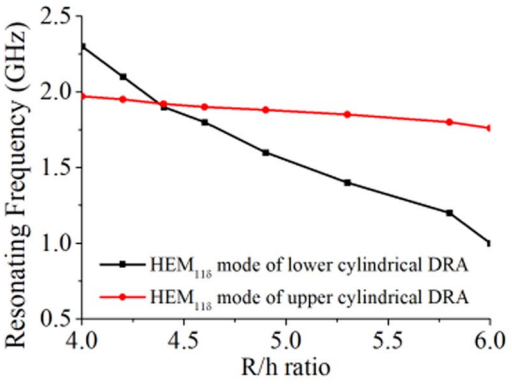


Figure 2. Simulated resonant frequencies versus R/h ratio of the bottom and top cylindrical DRAs.

Antenna design

Antenna structure

Figure 1 shows the configuration of the proposed L-band dual-CP antenna, which consists of double-layer dielectric, two radiation patches, two feeding probes with a radius of 0.15 mm and a ground plane. And its detailed dimension parameters are shown in the figure caption. As shown in Figure 1, each of the radiation patch consists of a circular radiator with several slender rectangular structures. The upper radiator generates RHCP radiation at higher frequency and the lower radiator generates LHCP radiation, respectively. The substrates chosen for this antenna are ceramic substrates with the dielectric constant of 14 ~ 16 (upper layer) and 7 ~ 9 (lower layer), respectively.

Working principle

The antenna's operation is based on a combination of the dielectric resonator antenna (DRA) and the microstrip antenna. The ceramic substrates with high dielectric constant laid on the ground can be taken as a cylindrical DRA working in $HEM_{11\delta}$ mode. As Figure 2 illustrates, the resonant frequencies of the cylindrical DRAs decrease as the ratio of R/h increases [19], which can be optimized to align the resonant frequency with the desired operating frequency. Figure 3 shows the influence of the circular patch covering the top of the dielectric. On the one hand, it can lower the resonant frequency by acting as a parallel capacitor. On the other hand, the patch itself works as a microstrip radiator and excites the TM_{01} mode. Therefore, as the patch radius increases, the working frequency of TM_{01} decreases. As a result, the frequency difference between the $HEM_{11\delta}$ and TM_{01} modes becomes smaller. Consequently, the impedance bandwidth is broadened when the two frequencies are brought close to each other.

Circular polarized properties

The slender rectangular structures on the circular radiator are presented to achieve CP radiation. Characteristic mode analysis (CMA) is employed to explain the operating principle. Figure 4 compares the simulated modal weighting coefficients (MWCs) excited by the feed probes for the configurations without and with the slender rectangular structures. As shown in Figure 4(a) and (c), the bottom feed probe (P1) only excites mode 4 while the top feed probe (P2) only excites mode 5 without the slender rectangular structures. However, with the introduction of the slender rectangular, P1 excites both modes 3 and 4 concurrently, and P2 excites both modes 5 and 6 simultaneously. According to the characteristic-mode theory in [20], circular polarization is obtained when two modes have analogous modal significance and phase difference close to 90°. As shown in Figure 5, the current directions of modes 3 and 4 are orthogonal at 1720 MHz, as well as modes 5 and 6 at 1810 MHz, which represents that the CP radiation can be achieved.

Parameters study

Key parameters are investigated to optimize the impedance matching and the CP performance listed in Table 1. First, as discussed

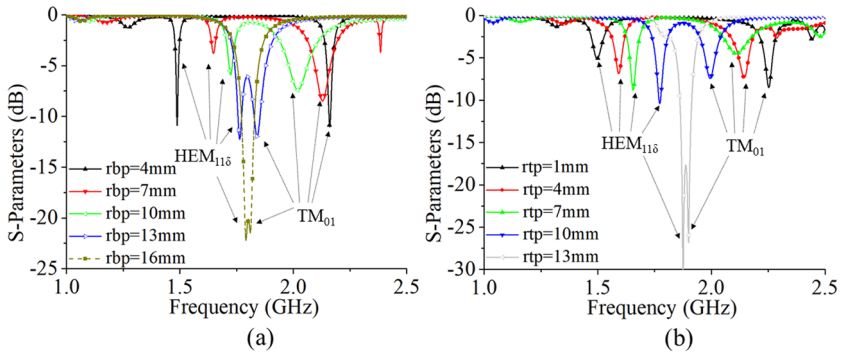


Figure 3. S-parameters versus frequency for different radius of (a) bottom patch and (b) top patch.

https://doi.org/10.1017/S175907872510281X Published online by Cambridge University Press

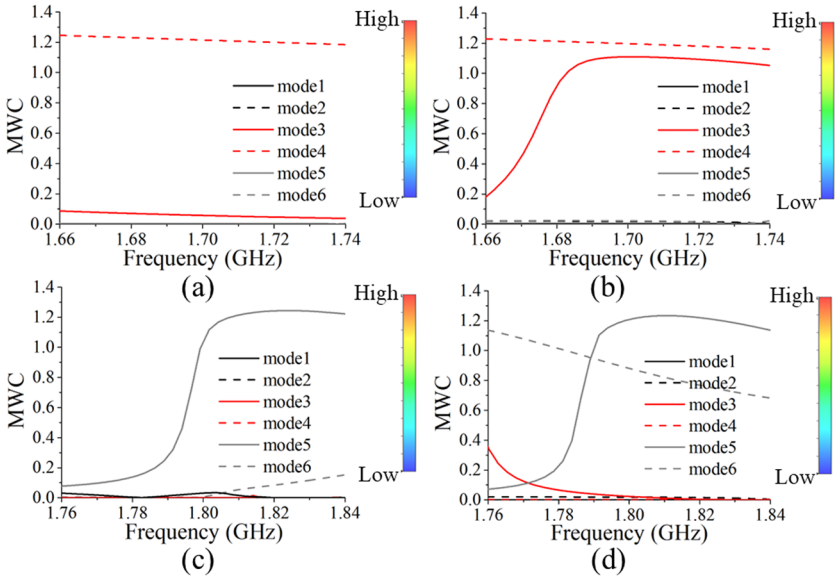


Figure 4. MWCs at 1720 MHz excited by P1 (a) without and (b) with slender rectangular structures. MWCs at 1810 MHz excited by P2 (c) without and (d) with slender rectangular structures.

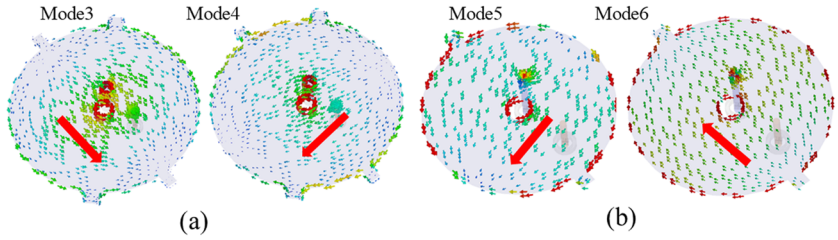


Figure 5. Modal surface currents at (a) 1720 MHz excited by P1 and (b) 1810 MHz excited by P2.

in Section B, the ratio of R/h and radius of patch are critical in determining the operating frequency. Consequently, the inherent resonant frequency of the bottom DRA is 1.81 GHz, and the operating band is 1.71–1.73 GHz when patch radiator covers the dieletric, while the top DRA resonates at 1.93 GHz and has an operating band of 1.80–1.82 GHz with patch radiator covered. Furthermore, the values of F_t and F_b could be adjusted to optimize the impedance matching for a better impedance bandwidth ($BW_{10\,dB}$). Second, the values of L1, L2, and L3, lengths of the slender rectangular structures on the circular radiators, are tuned to improve AR performance. As can be seen in Figure 6, increasing L1, L2, and L3 generally achieves a better AR but has a negligible impact on the impedance property. However, these lengths are constrained by the substrate radius, as the rectangular structures must maintain a sufficient distance from the substrate edge to ensure dimensional accuracy during fabrication. Therefore, L1, L2, and L3 are optimized for a tradeoff between the AR property and processing feasibility.

Simulated and measured results

To verify the performance of the design, a prototype was fabricated and measured. Figure 7 presents photographs of the prototype and a plot of the simulated and measured gain, AR, and reflection coefficients. The proposed antenna has an extremely small size of $0.005\lambda^3(0.29\lambda \times 0.29\lambda \times 0.06\lambda)$, making it particularly suitable as an array element with low inter-element coupling characteristics.

Table 1. Influences and values of the key parameters

Parameters	Optimization target	Values
$R_{t\text{-}s}/r_{tp}$	Resonant frequency of upper cylindrical DRA	5.84
$R_{b\text{-}s}/r_{bp}$	Resonant frequency of lower cylindrical DRA	4.69
r_{tp}	Working frequency of top element	12.2 mm
r_{bp}	Working frequency of bottom element	17.1 mm
F_t	Impedance matching of top element	4.3 mm
F_b	Impedance matching of bottom element	5.5 mm
L_1	CP performance of top element	29 mm
$L_2 \sim L_3$	CP performance of bottom element	40.8 mm 39 mm

The measured radiation efficiencies range from 57.6% to 67.2% in the downlink band and from 63.1% to 68.6% in the uplink band. And the measured $BW_{10\,dB}$ are 2.9% and 3.3% at downlink and uplink bands, respectively. The isolation between the low-band probe P1 and the high-band probe P2 exceeds 12 dB over the operating band. Owing to the high dielectric constant of ceramic substrate, the 3-dB axial ratio bandwidths are 1.2% and 0.83% at downlink and uplink bands, respectively. The measured gains are above 4.5 dBi, and the gain fluctuation is within 0.6 dB across the entire $BW_{10\,dB}$.

The 3-dB ARBW and radiation patterns are presented in Figure 8. For the down-link band at 1720 MHz, the measured

https://doi.org/10.1017/S1759078725102810X Published online by Cambridge University Press

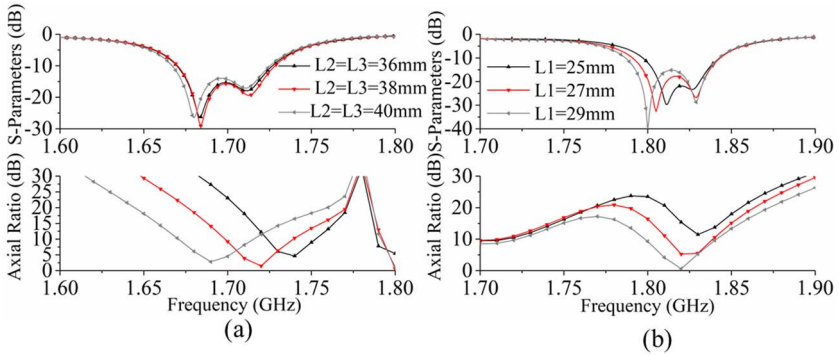


Figure 6. Effects of different values of L1, L2, and L3 on S-parameters and ARs of (a) bottom element and (b) top element.

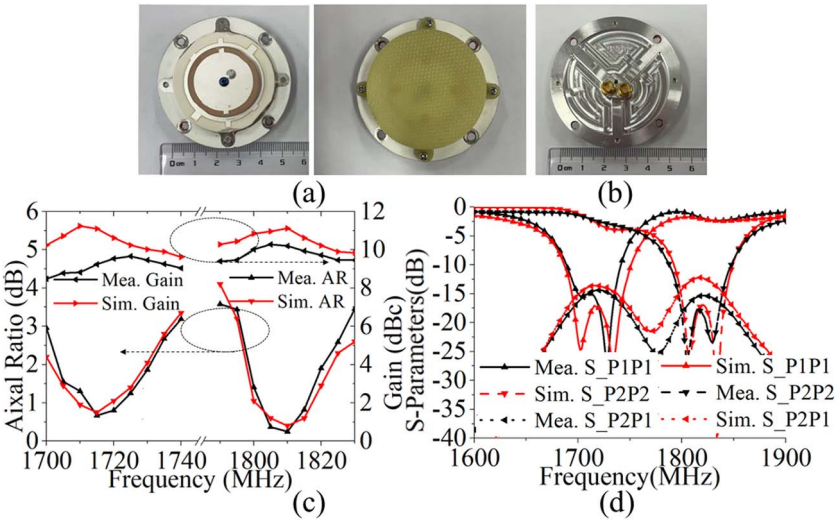


Figure 7. Photograph of fabricated antenna. (a) Top view without and with radome. (b) Back view. (c) Simulated and measured gain and AR. (d) S-parameters.

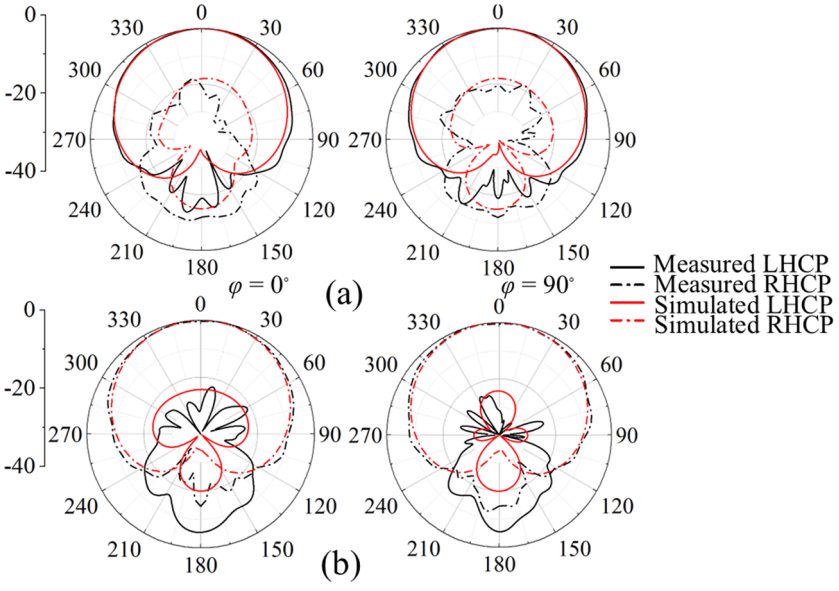


Figure 8. Simulated and measured radiation patterns at (a) 1720 MHz and (b) 1810 MHz. Simulated and measured results are in a relatively good agreement.

half-power beamwidths (HPBWs) are 98° at φ = 0° plane and 93°at φ = 90° plane, and the corresponding 3-dB ARBW are 160° and 167°, respectively. Similarly, for the up-link band at 1810 MHz, the HPBWs reach 101° at φ = 0° plane and 106° at φ = 90° plane, with 3-dB ARBW extending to 202° and 206°, respectively. Table 2 shows the performance comparison between other dual-CP antennas and the proposed antenna. It can be observed that among the listed designs, the proposed

https://doi.org/10.1017/S175907872510281X Published online by Cambridge University Press

Table 2. Comparison of the proposed and dual-CP reference antennas

Reference	Antenna type	FREQ (GHz)	Dimension (λ^3)	Gain (dB)	$BW_{10\ dB}$ (%)	3-dB AR bandwidth(%)	3-dB ARBW (deg)	HPBW (deg)	Isolation (dB)
[5]	Dipole	4	0.61	15	19	16.8	≥130	≥130	11
[8]	Microstrip	14.55	0.12	6	24.2	25	≥135	≥70	12
[13]	Microstrip	5.77/9.3	0.036	8.4/6.35	4.5/2.7	1.04/0.7	Not Given	≥60	Not given
[21]	Microstrip	1.176/1.575	0.61	3.68/3.31	2.5/2.7	1.5/1	Not Given	≥80	Not given
[22]	Microstrip	2.395/2.475	0.0051	5.46/5.46	7.95	0.33/0.72	≥74/≥188	NG	Not given
Proposed	Microstrip	1.72/1.81	0.005	4.4/4.7	2.9/3.3	1.2/0.83	≥160/≥202	93/101	12

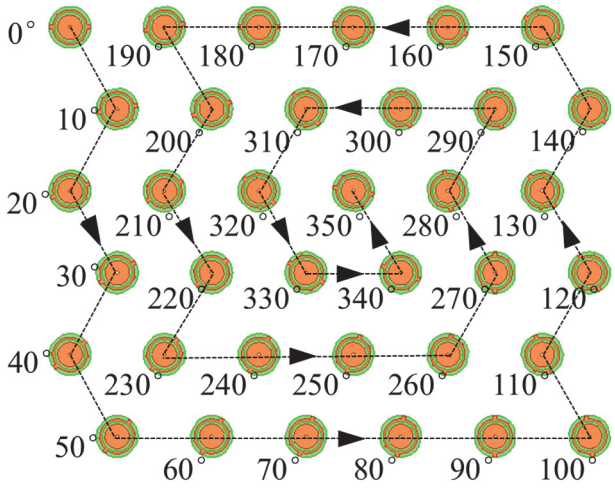


Figure 9. Layout and rotated angles of the 6 × 6spiral sequentially rotated L-band dual-CP microstrip antenna array.

antenna has both the widest 3-dB ARBW and the smallest size.

Array implementation and performance

Array configuration

The SSR can overcome the problem of high XPL and high SLL during wide-angle scanning by disrupting the periodic phase distribution [23]. In this paper, we composed the array using SSR as shown in Figure 9. The rotation angle is 360°/36. To improve the aperture efficiency, the elements are regularly arranged in a triangular configuration rather than a conventional square way, with an inter-element distance of 0.56λ at the highest resonance frequency of 1820 MHz. Correspondingly, the spacing between the array elements is about 0.52λ at the lowest frequency of 1710 MHz. For comparative analysis, we additionally simulated an SRT array, which was composed of 2 × 2 antenna subarrays with conventional sequential rotation angles of 0°, 90°, 180°, and 270°. Figure 10 shows the compensated phase matrices and as can be seen that there is a large and regular phase oscillation between 0° and 360° for SRT, while the phases of each element are scattering around the array of SSR, which could disrupt the periodic oscillation.

The RHCP/LHCP arrays demonstrate similar performance characteristics when employing the identical sequential rotation techniques. Taking the RHCP array as an example, the corresponding co-polarized (COP) and cross-polarized (XP) patterns at 1810 MHz are shown in Figure 11. When the antenna array was arranged in a square way, poor XPL at the diagonal-plane (D-plane, defined as φ = 45° plane) was a major issue for SRT [24]. However, the triangular configuration shifts this high XPL region to the H-plane (φ = 90° plane). It is evident from Figure 11(a) and (b) that when the main beam is steered to ($\theta = 50°, \varphi = 90°$). For the SRT array, the XP pattern exhibits prominent grating lobe in the H-plane with its level almost as high as the main lobe of COP. For the SSR array, the grating lobe in the H-plane has been eliminated while achieving a remarkable 12 dB improvement in cross-polarization suppression (from 4.1 to 16.1 dBc), which verifies the effectiveness of the SSR array to enhance the cross-polarization suppression.

Prototype and experimental result

To verify the simulated results, as shown in Figure 12, a 6 × 6-element low-profile dual-CP antenna array using the SSR technique was fabricated and measured. To evaluate the scanning performance, an RF network, which consists of a 1:36 power divider and 36 phase-shifters, is applied to provide required excitation phase of each element for beam steering after channel calibration. Figure 13 presents the measured S-parameters over operating frequency band. Only the isolations between the central array element (element E1 in Figure 12) and its adjacent elements (E2-E7) are measured, which are all larger than 22 dB. The measured patterns are shown in Figure 14 and summarized in Table 3.

The SSR can effectively solve the grating lobe problem in H-plane as mentioned before. For the down-link band at 1720 MHz, the measured XPLs at E-plane (φ = 0°), H-plane (φ = 90°), and D-plane (φ = 45°) are −19.8, −22.4, and −18.7 dB, respectively. Moreover, for the up-link band at 1810 MHz, the measured XPLs at E-plane, H-plane, and D-plane are −18.1, −19.6, and −19.2 dB, respectively. The simulated and measured axial ratio and boresight gain versus beam steering are presented in Figure 15, while Figure 16 shows the cross-polarization suppression and radiation efficiency versus frequency. The proposed array can maintain the boresight gain fluctuation within 1.6 dB over the operating frequency band and the scan loss at θ = 55° is less than 4 dB. For the low-band probe, the measured gain is between 17.46 and 18.64 dB, with cross-polarization suppression between 23.2 and 28.8 dBc. Meanwhile, for the high-band probe, the corresponding values are 18.4–19.03 dB for gain and 24.7–31.2 dBc for suppression. Additionally, its 3-dB AR scanning angle was from −55° to +55° over the operational band, which has a good CP wide-angle scanning characteristic. Furthermore, the measured radiation efficiencies during beamforming are 52.2%–59.3% in the downlink and 56.6%–64.1% in the uplink bands, which are slightly lower than that of a single antenna due to the coupling losses.

https://doi.org/10.1017/S175907872510281X Published online by Cambridge University Press

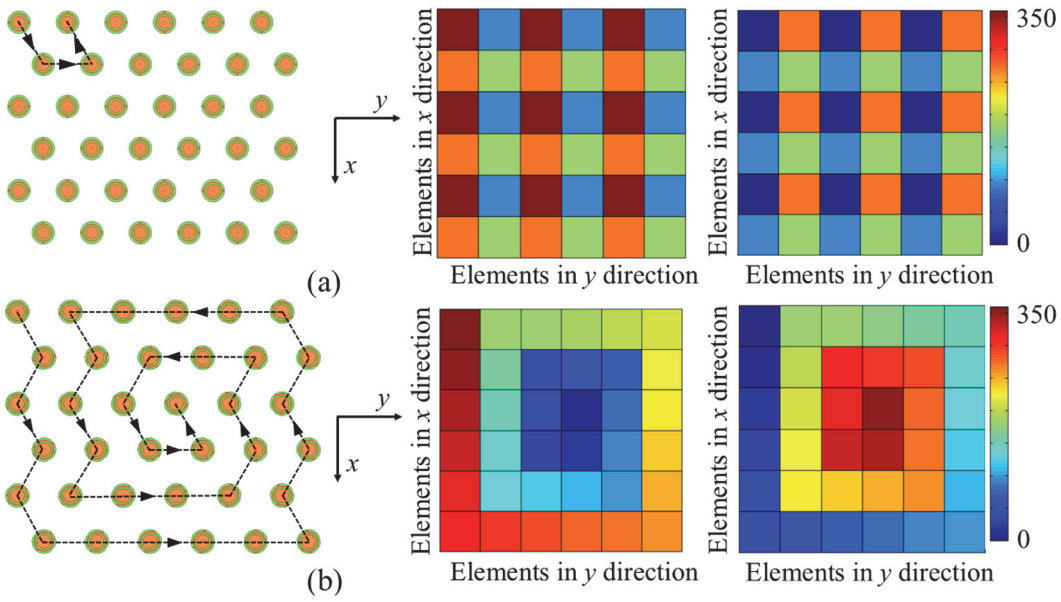


Figure 10. Representation of layout and compensated phase matrices at 1720 and 1810 MHz on (a) the conventional SRT and (b) the SSR.

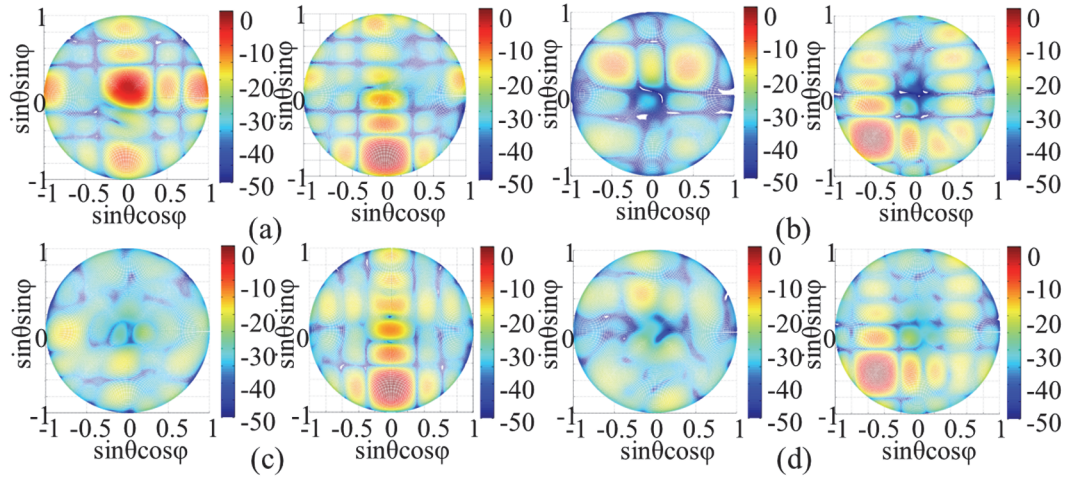


Figure 11. Top views of the full-wave simulated XP and COP patterns when the main beam is steered to (a) $\theta = 50°$, $\varphi = 90°$, (b) $\theta = 50°$, $\varphi = 45°$ by the SRT, and (c) $\theta = 50°$, $\varphi = 90°$, (d) $\theta = 50°$, $\varphi = 45°$ by the SSR at 1810 MHz.

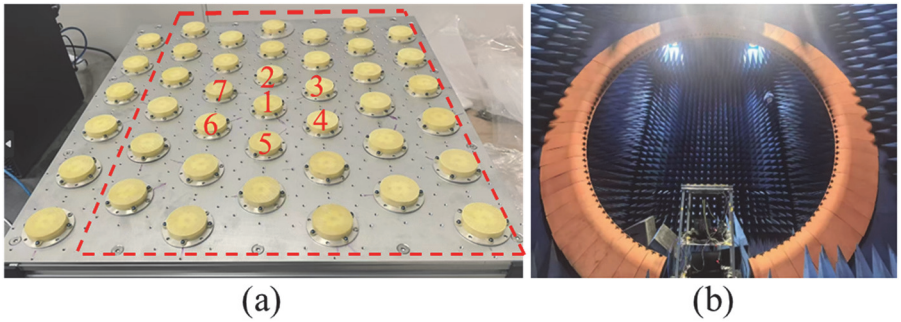


Figure 12. Photograph of (a) fabricated 36-element L-band dual-CP SSR array and (b) measurement scenario.

Finally, a comparison between our work and previous dual-CP for wide-scanning works is provided in Table 3. In contrast, our proposed array has the lowest profile as well as XPL over the 3-dB scanning angle. All the merits make our proposed dual-CP array an attractive candidate for the wide-angle coverage satellite system. However, as these systems typically employ frequency-division duplexing and the third-order inter-modulation product falls close to the received band, it is recommended to use transceiver filters connected after the antenna to suppress interference effectively.

https://doi.org/10.1017/S175907872510281X Published online by Cambridge University Press

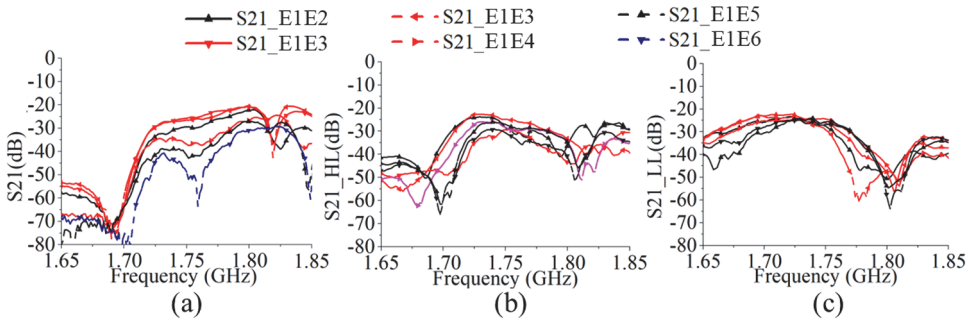


Figure 13. Measured S-parameters of (a) high-band probes and high-band probes, (b) high-band probes and low-band probes, and (c) low-band probes and low-band probes over working frequency.

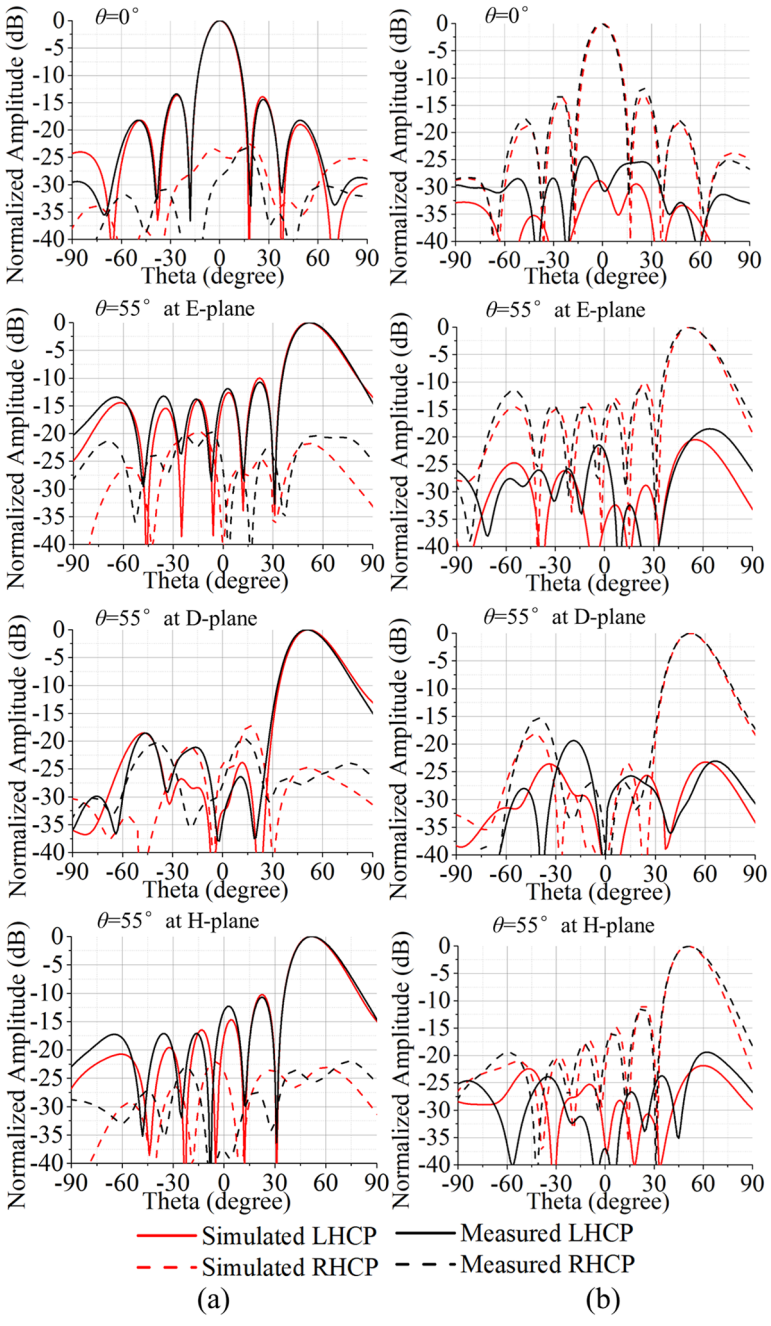


Figure 14. Measured and simulated radiation patterns versus beam steering at (a) 1720 MHz and (b) 1810 MHz. Simulated and measured results are in a good agreement.

https://doi.org/10.1017/S1759078725102810X Published online by Cambridge University Press

Table 3. Comparison of the proposed and reference dual-CP arrays

Reference	Antenna Type	Array Size	Scan bandwidth (%)	Freq (GHz)	Profile (λ)	Scanning angle AR ≤ 3 dB (deg)	Gain loss (dBc)	XPL (dB)	SLL (dB)
[6]	Waveguide	2 × 4	7.4	4.05	0.8	±40	≤3 dB	NG	≤−10
[7]	Microstrip	2 × 2	14.3/10.9	13/18	0.12	±26/ ± 16	NG	≤−10	−5.1/−7.8
[8]	Microstrip	1 × 8	4.8	14.55	0.09	−59 ~ 58	≤3.2 dB	NG	≤−5
[9]	Microstrip	2 × 8	2.5/1.7	19.95/29.75	0.25	±55	≤4.1 dB	≤−10	≤−7
[10]	Microstrip	8 × 8	14	25	0.11	±51/ ± 36	≤3 dB	≤−10	≤−7
[11]	Microstrip	1 × 8	10.5/2.8	2.1/2.492	0.1	25 ~ 55/7 ~ 55	≤2.5 dB	NG	≤−10
Proposed	Microstrip	6 × 6	2.9/3.3	1.7/1.8	0.06	±55	≤4 dB	≤−18.1	≤−10

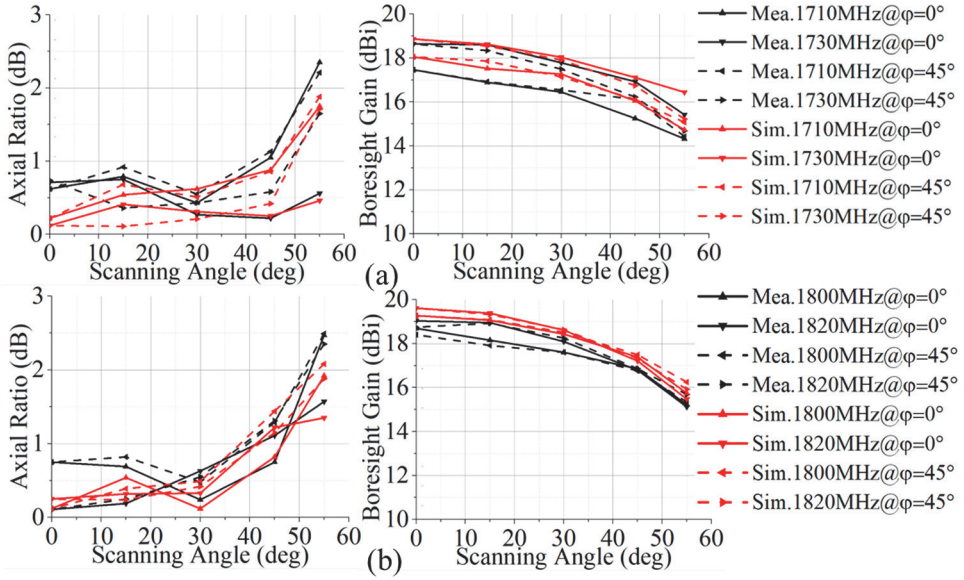


Figure 15. Simulated and measured (a) axial ratio and (b) boresight gain versus beam steering.

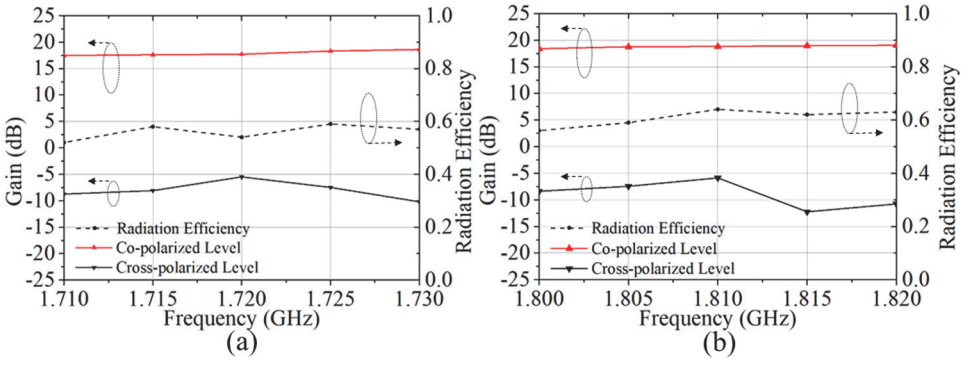


Figure 16. Co-/cross-polarization gain (dBi) and radiation efficiency versus frequency over (a) downlink band and (b) uplink band.

Conclusion

A low-profile dual-CP antenna array using the SSR technique is proposed for satellite communication in this work. The array element consists of two stacked CP patches and double-layer ceramic substrate with high dielectric constant. Dual CP radiations are accomplished by the slender rectangular structures on the radiators, which can excite two orthogonal characteristic modes. Moreover, extremely small size of $0.005\lambda^3$ and wide 3-dB ARBW of 206° are achieved. Furthermore, a prototype of a 6 × 6 SSR array was fabricated and measured. Measured results show that a wide 3-dB AR scanning angle of ± 55° is realized for LHCP as well as RHCP radiation. Additionally, low XPL less than −18.1 dB with gain fluctuation less than 4 dB are achieved over −55° ~ + 55°. All the merits of dual-CP radiation, ultra-low profile, wide 3-dB AR scanning angle, and low XPL make our proposed dual-CP SSR array be highly attractive candidate for satellite communication applications.

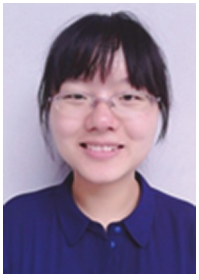
https://doi.org/10.1017/S175907872510281X Published online by Cambridge University Press

Acknowledgements. The authors declare no competing interests.

Funding. This work was supported by the CAS Key Technology Talent Program under Grant E0293006.

References

1. **Checcacci P and Spalla P** (1976) Analysis and correction of errors in a polarimeter for Faraday rotation measurements. *IEEE Transactions on Antennas and Propagation* **24**, 253–255. https://doi.org/10.1109/TAP.1976.1141306.
2. **Volakis JL** (2007) *Antenna Engineering Handbook*. New York, NY, USA: McGraw-Hill.
3. **Zhang L Yin J, Kong Z, Wang Y, Zhu K, He Y and Sun H** (2024) Sextuple-band circularly polarized shared-aperture antenna for navigation and wireless communication. *IEEE Antennas and Wireless Propagation Letters* **23**, 4353–4357. https://doi.org/10.1109/LAWP.2024.3445669.
4. **Feng B, Li L, Chung KL and Li Y** (2021) Wideband widebeam dual circularly polarized magnetoelectric dipole antenna/array with meta-columns loading for 5G and beyond. *IEEE Transactions on Antennas and Propagation* **69**, 219–228. https://doi.org/10.1109/TAP.2020.3008632.
5. **Li M, Su Y, Yao Y, Zhang W, Lin X and Fan Y** (2024) A broadband dual-polarized C-/Ku-band shared aperture antenna array for satellite communications. *IEEE Transactions on Antennas and Propagation* **72**, 8840–8845. https://doi.org/10.1109/TAP.2024.3439827.
6. **Xia L-X, Liu N-W, Zhu L and Fu G** (2024) Dual-CP antenna with wide-HPBW and wide-ARBW performance for wide-angle scanning phased array. *IEEE Transactions on Antennas and Propagation* **72**, 4583–4588. https://doi.org/10.1109/TAP.2024.3373064.
7. **Liu W, Cao Y, Chen J and Yan S** (2024) Design of a low-profile dual-band shared-aperture circularly polarized phased array. *IEEE Antennas and Wireless Propagation Letters* **23**, 543–547. https://doi.org/10.1109/LAWP.2023.3329153.
8. **Wei CY, Hao Chi Zhang, Pei Hang He, Le Peng Zhang, Xiao Tian Yan, Jiayuan Lu and Tie Jun Cui** (2022) A dual circularly polarized SIW-fed phased array antenna with wide-angle beam scanning range. *IEEE Transactions on Antennas and Propagation* **70**, 7393–7402. https://doi.org/10.1109/TAP.2022.3177939.
9. **Chang X, Wang HB, Li TJ, Jin SC, Liu DG and Cheng YJ** (2022) Shared-aperture phased array antenna with codesigned near-field coupled circular polarizer loaded for K/Ka-band wide-angle satellite communication. *IEEE Transactions on Antennas and Propagation* **70**, 7478–7490. https://doi.org/10.1109/TAP.2022.3196619.
10. **Das S, Sharma Sk, Waldstein SW, Downey Jm, Schoenholz BL, Dever SM, Nessel JA and Banerjee R** (2023) A flat-panel 8 × 8 wideband K-/Ka-band dual circularly polarized phased array antenna for CubeSat communications. *IEEE Transactions on Antennas and Propagation* **71**, 4153–4166. https://doi.org/10.1109/TAP.2023.3255640.
11. **Zhang L, Lin F, Sun HJ and Yin JY** (2024) A wide-angle scanning circularly polarized shared- aperture array with low scan loss capability. *IEEE Antennas and Wireless Propagation Letters* **23**, 2880–2884. https://doi.org/10.1109/LAWP.2024.3412889.
12. **Yan D, Jiao C, Cheng H-T and Zhang C** (2021) A low-profile dual-circularly polarized wide-axial-ratio-beamwidth slot patch antenna with six-port feeding network. *IEEE Antennas and Wireless Propagation Letters* **20**, 2486–2490. https://doi.org/10.1109/LAWP.2021.3115802.
13. **Ji S, Dong Y, Wen S and Fan Y** (2021) C/X dual-band circularly polarized shared-aperture antenna. *IEEE Antennas and Wireless Propagation Letters* **20**, 2334–2338. https://doi.org/10.1109/LAWP.2021.3110529.
14. **Zhang X, Zhu L and Liu N-W** (2017) Pin-loaded circularly-polarized patch antennas with wide 3-dB axial ratio beamwidth. *IEEE Transactions on Antennas and Propagation* **65**, 521–528. https://doi.org/10.1109/TAP.2016.2632728.
15. **Luo Y, Chu Q-X and Zhu L** (2015) A miniaturized wide-beamwidth circularly polarized planar antenna via two pairs of folded dipoles in a square contour. *IEEE Transactions on Antennas and Propagation* **63**, 3753–3759. https://doi.org/10.1109/TAP.2015.2438334.
16. **Huang J** (1986) A technique for an array to generate circular polarization with linearly polarized elements. *IEEE Transactions on Antennas and Propagation* **34**, 1113–1124. https://doi.org/10.1109/TAP.1986.1143953.
17. **Hall PS and Smith MS** (1994) Sequentially rotated arrays with reduced sidelobe levels. *IEE Proceedings - Microwaves, Antennas and Propagation* **141**, 321–325. https://doi.org/10.1049/ip-map:19941193.
18. **Smolders AB and Johannsen U** (2011) Axial ratio enhancement for circularlypolarized millimeter-wave phased-arrays using a sequential rotation technique. *IEEE Transactions on Antennas and Propagation* **59**, 3465–3469. https://doi.org/10.1109/TAP.2011.2161443.
19. **Deyoung CS and Long SA** (2006) Wideband cylindrical and rectangular dielectric resonator antennas. *IEEE Antennas and Wireless Propagation Letters* **5**(1), 426–429. https://doi.org/10.1109/LAWP.2006.883952.
20. **Garbacz RJ** (1965) Modal expansions for resonance scattering phenomena. *Proceedings of the Institute of Electrical and Electronics Engineers* **53**8, 856–864. https://doi.org/10.1109/PROC.1965.4064.
21. **C S, M ND and M J** (2022) Dual-band circularly polarized annular ring patch antenna for GPS-aided GEO-augmented navigation receivers. *IEEE Antennas and Wireless Propagation Letters* **21**, 1737–1741. https://doi.org/10.1109/LAWP.2022.3178980.
22. **Zhao Z, Liu F, Ren J, Liu Y and Yin Y** (2020) Dual-sense circularly polarized antenna with a dual-coupled line. *IEEE Antennas and Wireless Propagation Letters* **19**, 1415–1419. https://doi.org/10.1109/LAWP.2020.3003943.
23. **Kang Z, He L, Xiao Y and Liang G** (2025) Low cross-polarization level circularly-polarized phased arrays using a spiral sequential rotation technique. *IEEE Antennas and Wireless Propagation Letters* https://doi.org/10.1109/LAWP.2025.3557268.
24. **Smith MS** (1991) Grating lobes of sequentially rotated antenna arrays. *Seventh International Conference on Antennas and Propagation, ICAP 91(IEE),* York. pp 217–220.



Zhanyu Kang is with the Innovation Academy for Microsatellites, Chinese Academy of Sciences (IAMCAS), Shanghai 201304, China, and also with the University of Chinese Academy of Sciences (UCAS), Beijing 100049, China (e-mail: bbpp-shiwo@126.com).



Lianxing He is with the Innovation Academy for Microsatellites, Chinese Academy of Sciences (IAMCAS), Shanghai 201304, China (e-mail: 13816474811@139.com).



Dongliang Fei is with the Innovation Academy for Microsatellites, Chinese Academy of Sciences (IAMCAS), Shanghai 201304, China (e-mail: feidl@microsate.com).



Guang Liang is with the Innovation Academy for Microsatellites, Chinese Academy of Sciences (IAMCAS), Shanghai 201304, China (e-mail: hnlg219@163.com).



Shaokang Pan is with the School of Information Science and Technology, ShanghaiTech University, Shanghai 201210, China, and also with the Innovation Academy for Microsatellites, Chinese Academy of Sciences (IAMCAS), Shanghai 201304, China. (e-mail: panshk@shanghaitech.edu.cn).

https://doi.org/10.1017/S175907872510281X Published online by Cambridge University Press